An exploratory study of shielding strategies for boron neutron capture discrimination in ^{10}B Neutron Capture Enhanced Particle Therapy

Marissa Kielly[a,b], Andrew Chacon[a], Anita Caracciolo[c,d], David Bolst[b], Anatoly Rosenfeld[b], Marco Carminati[c,d], Carlo Fiorini[c,d], Daniel R. Franklin[e], Susanna Guatelli[b], Mitra Safavi-Naeini[a,*]

[a]*Australian Nuclear Science and Technology Organisation (ANSTO), Lucas Heights, Australia*
[b]*Centre for Medical Radiation Physics, University of Wollongong, Wollongong, Australia*
[c]*Dipartimento di Elettronica, Informazione e Bioingegneria, Politecnico di Milano, Milano, Italy*
[d]*Istituto Nazionale di Fisica Nucleare (INFN), Sezione di Milano, Milano, Italy*
[e]*School of Electrical and Data Engineering, University of Technology Sydney, Ultimo, Australia*

Abstract

Purpose: To evaluate the impact of a range of shielding strategies on the rate of false positive detections by a simulated detector for application in Neutron Capture Enhanced Particle Therapy (NCEPT).
Methods: In this work, we extend a previously published method for neutron capture detection and discrimination. A Geant4 Monte Carlo model was designed, with the simulated irradiation of a poly(methyl methacrylate) phantom and cubic ^{10}B insert with carbon and helium ion beams and various shielding configurations.
Results: In the free-space configuration, shielding the crystal actually decreases the ratio of true/false positive detections (R_{TF}) by more than 50% and increases the activation of the detector. In a closed-space configuration with a model of the beamline neutron fluence, R_{TF} also decreases with shielding, although activation decreases in this case. However, for a detector with boron present in the printed circuit boards (PCBs), shielding with a thin layer of Gd_2O_3 improves R_{TF} by up to 21%.
Conclusions: Shielding of the detector crystal itself is unnecessary as shielding actually degrades discrimination accuracy relative to the unshielded detector. However, if the detector PCBs contain boron, then shielding the electronics provides a valuable increase in overall detector selectivity.

Keywords: Geant4, Monte Carlo, Neutron shielding, Neutron capture, Prompt gamma

1. Introduction

Neutron Capture Enhanced Particle Therapy (NCEPT) boosts the therapeutic benefits of heavy ion therapy through dose enhancement from neutron capture [1, 2]. By utilising tumour-specific neutron capture agents (NCAs) containing either ^{10}B or ^{157}Gd, internally generated thermal neutrons can be captured, increasing dose to the target volume. The resulting processes produce high-LET particles and signature gamma photons, such as 478 keV photons for ^{10}B capture.

Quantifying the total dose in NCEPT is challenging since it consists of two main components: (1) the dose from the incident ion beam and (2) the neutron capture dose. As the neutrons are both generated and captured internally, directly quantifying the second component is difficult, yet critical to estimating total dose to the target [3, 4]. Therefore, developing a comprehensive dose monitoring system is necessary for clinical translation of NCEPT. Ultimately, the efficacy of the dose monitoring system depends on an accurate differentiation of neutron capture photons from the background.

Our previous work proposed exploiting temporal and spectral signatures of the neutron-capture photons to quantify neutron capture events in real-time during NCEPT treatments [3]. We investigated preliminary detector concepts to

*Corresponding author.
Email address: mitras@ansto.gov.au (Mitra Safavi-Naeini)

demonstrate their potential for real-time dose monitoring [4]. This work also showed that neutrons, especially those of intermediate energies between 1 eV and 1 MeV, can deposit energy in the detector within the same timing and energy windows as the neutron capture photons, obscuring the neutron capture signal by creating false positive detections [3]. More recently, we have demonstrated the ability of the prototype BeNEdICTE detection system to detect an increase in the 478 keV spectral signature during irradiation of a boron bolus within a PMMA phantom [4]. However, the system also exhibited a substantial false positive rate due to neutrons interacting with boron present in the detector electronics. Additionally, there is a prompt gamma background spectrum which results from short-lived nuclear excited states, including 4.44 MeV and 6.13 MeV photons from ^{12}C and ^{16}O, respectively [5, 6, 7].

In this work, we explore shielding solutions which aim to minimise the incidence of background neutrons and photons reaching the detector. The goal is to determine whether shielding can improve detector selectivity, defined as the ratio of true neutron capture detections to false positives (R_{TF}), without compromising its sensitivity. In addition to this, the impact of shielding on detector activation is also considered; an appropriate shielding configuration should decrease the intensity of activation lines from neutron interactions with the detector.

Shielding configurations for neutrons frequently employ hydrogen-rich materials, such as polyethylene or paraffin, due to their high elastic scattering cross-section, which enables effective neutron moderation [8]. For polyenergetic neutron fields, shielding layers with high thermal neutron capture cross-sections are often used. Mixed materials such as borated polyethylene or polyethylene/B_4C composites can also be used to moderate higher energy neutrons and capture them at thermal temperatures [9, 10]. However, shielding materials containing boron cannot be used for ^{10}B NCEPT, since dose quantification relies on accurate measurement of the number of photons being emitted during the boron neutron capture process. Additionally, high atomic number elements, such as tungsten or lead, are commonly used for shielding and collimation in prompt gamma detection applications [11, 12, 13, 14, 9]. Here, we optimise the composition and geometry of a heterogeneous layered shielding structure with the goal of maximising the ratio of true positive to false positive neutron capture detections.

This paper consists of the following sections: the simulation configuration, methods, and metrics are described in Section 2, the results are presented in Section 3 and discussed in Section 4 and finally, Section 5 provides a conclusion on the outcome of this study and suggestions for further investigation and potential experimental work.

2. Materials and Methods

The effect of shielding on the selectivity of the detector and its neutron activation is evaluated with several different shielding configurations, with and without concrete walls, and with and without a printed circuit board (PCB) behind the detector, for both carbon and helium ion beams.

Two shielding configurations are considered; firstly, a multilayer shield designed via an optimisation process, and secondly, a simplified design which eliminates materials that may be too heavy or expensive to include in a prototype. In this study, these materials are compared to the no-shielding case for three different detector materials - CdTe, CZT and $LaBr_3$(Ce) - through their impact on both the ratio of true to false positive neutron capture detections (R_{TF}) and the activation of detector materials. The evaluation is first performed with both carbon and helium ion target irradiation for a perfect case of no scattering in the room (e.g. from surrounding walls) and no neutron background from the beamline. A second evaluation is then performed for the carbon ion beam only, in which the model is extended to include the walls and ceiling as well as additional neutron fluence from the beamline, to determine the effect of scattered particles on the false positive count rate in the detector.

The PCB of the BeNEdiCTE prototype detector is known to contain boron, which contributes to false positive detections when in the presence of a high neutron background [4]. To investigate the impact of these false positives on R_{TF}, the PCB was also modelled in a third configuration with simple shielding of lead and Gd_2O_3 or cadmium.

From these results, the most appropriate shielding configuration and detector material will be proposed for ^{10}B NCEPT.

2.1. Geant4 simulation design and configuration

Geant4 version 11.0 is used throughout this work [15] and the properties of all materials are as defined by the National Institute of Standards and Technology (NIST) in Geant4 [16]. Electromagnetic physics interactions were modelled using the `G4EmStandardPhysics_option3`, while the High Precision model and Binary Ion Cascade (BIC)

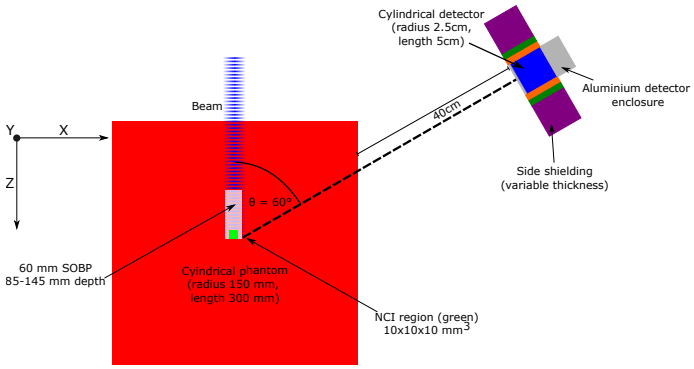

(a) Full schematic for the phantom and detector simulation configuration

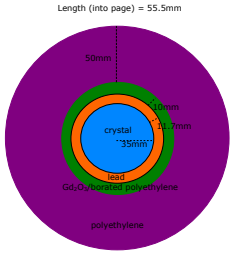

(b) Front view of the detector and side shielding simplified configuration

Figure 1: Schematics for the Monte Carlo simulations

were used for neutron and hadronic inelastic nuclear interactions, respectively. A complete table of the physics models used in the simulation is included in the Supplementary Materials as Table S1. The simulations conducted for this study do not currently model optical scintillation; the detector output is assumed to be proportional to the energy deposited in the crystal.

A cylindrical poly(methyl methacrylate) (PMMA) phantom was modelled in the simulation, with a radius of 150 mm and a length of 300 mm in the z-direction parallel to the beam (see Figure 1(a)). A 10 mm^3 pure ^{10}B cubic insert was then centred in the x-y plane and positioned at a depth of 140 mm in the phantom, so as to sit at the distal end of the 60 mm spread out Bragg peak (SOBP) generated by primary ^{12}C or ^{4}He ion beams.

The ion beams have a circularly symmetric Gaussian profile with FWHM of 20 mm and were generated normal to the surface of the phantom with particle energies of 225-294 MeV/u for carbon ions and 113-156 MeV/u for helium ions. The process for the synthesis of these beam spectra is described by Safavi-Naeini et al. [2], and models the biological beamline at the Heavy Ion Medical Accelerator in Chiba (HIMAC), Japan.

The detector model is based on the design of the BeNEdiCTE module [17]; the sensitive volume is a 50 mm×50 mm cylindrical crystal of $LaBr_3$(Ce), CZT or CdTe, surrounded by a cylindrical aluminium enclosure with a thickness of 6.5 mm and radius of 35 mm. It is assumed that in practice, CZT and CdTe-based detectors would consist of a stack of detectors coupled to form a single unit with the same dimensions as the solid $LaBr_3$(Ce) crystal. This assumption was also made to enable easier comparison to our previous work in Chacon et al.[3].

The detector is positioned at an angle of 60° with respect to the beam in the forward-facing direction and proximal to the Bragg peak, as shown in Figure 1(a). The front face of the detector is oriented normal to the neutron capture insert at a distance of 40 cm from the phantom, to reduce the number of neutrons directly interacting with the detector, since secondary neutrons are primarily created with forward momentum parallel to the beam [18, 19]. Each of the chosen detector materials, $LaBr_3$(Ce), CZT and CdTe, provide high energy resolution; the relevant physical characteristics of each material are included in Table 1[1]

For the initial study, a total of 5×10^9 particle histories were simulated for each beam type (carbon and helium ions). Particles arriving at the detector volume (comprising the shielding and detector module) were saved in a phase-space file to minimise computational time; this phase space file contains information about all particles entering this volume, including energy, time of arrival, position, and momentum. All variations in detector material and shielding configuration were then evaluated using the same phase-space files. For each energy deposition event inside the detector, the following was recorded:

- Time of arrival;
- Particle type;

[1]The BeNEdiCTE module has a codoped $LaBr_3$(Ce+Sr) crystal. This study utilises a cerium-doped crystal so as to match our previous simulation study.

Table 1: Detector materials evaluated in this study.

Material	Density (g/cm^3)	Yield (ph/keV)	Decay time (ns)	Energy resolution (%)	Emission wavelength (nm)	Data source
$LaBr_3$(Ce)	5.06	63-73	16-25	2.2-2.7	380-385	[20, 21, 17]
CdTe	5.85	N/A (direct)	N/A (direct)	2.4	N/A (direct)	[22]
CZT	5.8	N/A (direct)	N/A (direct)	2-3	N/A (direct)	[23]

- Total energy deposition;
- Charge;
- Position;
- Original volume; and
- Original energy.

For each of the evaluated conditions, the phase-space file was run to create 20 populations, with particle histories run until doubling the number of particles did not decrease the ratio of standard deviation to the mean by more than 10% for the R_{TF}.

2.1.1. Temporal masking

Total irradiation times of 1 μs, 10 μs, 100 μs, 1 ms, 10 ms and 100 ms were simulated for each ion beam, with a macroscopic beam pulse period of 200 ns and a beam-on period of 11 ns (i.e., a duty cycle of 5.5%); this matches the temporal beam structure at HIMAC [24, 25]. Several temporal masks were applied to differentiate neutron capture photons from the prompt gamma background, based on our previous work [3]. Masks were applied from the start of each 200 ns nano-spill; the following durations were evaluated:

- 0 ns - no mask;
- 11 ns - the beam-on time;
- 22 ns - the beam-on time plus an additional 11 ns to allow for prompt gamma emission and arrival of photons at the detector [3]; and
- 30, 40, 50, 60, 70, 80, 90, 100, 110, 120 and 130 ns - additional periods to investigate the changes in emission over time. 110-130 ns temporal masks were only applied for the helium ion beam.

2.2. Performance metrics

2.2.1. Detector selectivity (R_{TF})

The primary performance metric used in this work is the true:false positive ratio (R_{TF}), which is determined for each beam and shielding configuration. These classifications were assigned from the timing and energy characteristics of each event, as well as the process that created it, as recorded in the Geant4 simulation. In this work, the definitions for true and false positive events are consistent with those used by Chacon et al. [3]:

- True positives: events which originated from neutron capture inside the neutron capture insert and are detected during the energy and temporal acceptance windows. These are determined in Geant4 only by including photons where the original volume is the insert and the energy is equal to 478 keV for ^{10}B, while considering the energy resolution of the detector;
- False positives: events which are detected within these windows, but which arise from processes other than neutron capture. This includes all other photons detected which were not created inside the insert region or had undergone Compton scattering.

All confidence intervals shown on the figures and included in the R_{TF} calculations are for ±2 standard errors (95%).

2.2.2. Detector activation

The activation of the detector following irradiation during NCEPT was also evaluated with and without shielding. Since activation can create long-lived radioisotopes, events which occur due to neutron interactions inside the detector after 4 days (3.5×10^{14} ns) [2] were scored and their spectra were plotted with 10 keV linearly spaced energy bins. These isotopes will accumulate over time and will therefore contribute to background radiation in the detector.

2.3. Shielding optimisation

The optimisation was achieved in two steps. First, the performance of eight individual candidate shielding materials were evaluated with respect to layer thickness and neutron energy band; then, a quadratic programming optimisation method was used to determine the optimal combination of shielding materials subject to the spatial constraints of the detector.

2.3.1. Single layer shielding evaluation

Simulations were conducted to evaluate the performance of individual candidate layers as a function of layer thickness in different neutron energy bands. For each shielding material tested, a 500 mm×500 mm square layer and a thickness varying between 5 mm and 25 mm for neutron capture materials and between 10 mm and 50 mm for moderating materials was constructed. A square neutron beam of size 50 mm×50 mm was simulated at the centre and on the surface of the shielding layer. The neutron beam spectrum was based on the results obtained in previous work [3], i.e., the spectrum of neutrons leaving a PMMA phantom during carbon or helium ion beam irradiation.

Eight candidate materials were considered based on their previously reported use in shielding applications: polyethylene, polycarbonate, water, aluminium, tungsten, gadolinium oxide (Gd_2O_3), gadolinium (metal), and hafnium [3].

The fluence of transmitted neutrons across seven energy bands are scored and summed individually for each band using a 500 mm×500 mm×1 mm ideal detection plane, placed immediately distal to the shield, and compared to the no-shielding case. This volume consisted of air, with all neutrons incident on the front face of the plane at any position summed to give the total neutron fluence in each band. The energy bands are:

- thermal neutrons; KE $\leq$ 0.4 eV
- 1 < KE < 10 eV
- 10 < KE < 100 eV
- 100 eV < KE < 1 keV
- 1 keV < KE < 100 keV
- 100 keV < KE < 1 MeV
- fast neutrons; KE $\geq$ 1 MeV

The ratio of intensity $I(x)$ for shielding thickness x and the fluence per primary neutron if the shielding layer is not present, $I(0)$, were calculated, and the macroscopic cross-section:

$$\Sigma(x) = -\frac{\log \frac{I(x)}{I(0)}}{x} \tag{1}$$

was plotted as a function of layer thickness x for each energy band across all evaluated thicknesses. $\Sigma(x)$ is well-approximated as a linear function; a line of best fit was calculated for each material in each energy band and the parameters were recorded.

The energy of any photons reaching the detector plane was also recorded. As the primary aim of the shielding is to increase R_{TF}, an increase in the number of photons which deposit their energy within the 478 keV neutron-capture window must be evaluated to determine the impact, if any, on the false positive rate.

[2] This time was chosen so as to ensure that all interactions between the ion beam and the detector had occurred.

[3] As the addition of materials containing the same element as the NCA would increase the number of false positives from neutron capture in the shielding, boron-containing materials are not considered for ^{10}B NCEPT.

2.3.2. Multi-layer shield optimisation

The linear model parameters for each material and neutron energy band were used as inputs for the design of an optimal multi-layer shield, subject to geometric constraints imposed by the detector geometry. The optimisation process was performed using the interior-point convex algorithm in the MATLAB quadprog (quadratic programming) solver [26].

The quadratic solver was used to determine the combination of shielding materials and their respective thicknesses which minimises the neutron fluence at the detector. The cost function was weighted to most heavily penalise the contribution of intermediate-energy neutrons (given a total weighting of 0.8, divided equally between each of the five middle bands, since these neutrons have the greatest detrimental impact on R_{TF}), followed by thermal and fast neutrons (with a weighting of 0.1 each). A negative cost term with a weighting of (-)0.1 was added for photon attenuation μx at 478-keV (assuming an energy resolution of 3%), which seeks to maximise photon attenuation from the shielding layers, since 478 keV photons entering from the side only contribute to false positives. Finally, the number of photons emitted per unit thickness of the shielding material that are within the 478 keV energy window (again, assuming a 3% energy resolution) was determined and added to the total cost with a weighting factor of 10 to severely penalise materials that will excessively contribute to false positive counts through neutron activation of the shielding.

In addition to the fully-optimised multi-layer shield, a simplified alternative was developed using only cheaper and lighter materials. An additional layer of 1.17 cm of lead (equal to the one-tenth value layer, or TVL, for 478 keV photons) was added to both configurations for additional photon shielding.

Optimal combinations (both the fully optimised multi-layer shield and the simplified shield) were simulated in Geant4 to determine the neutron fluence ratios (calculated as previously discussed for single layer shielding). 20 populations of 5×10^6 neutron histories were simulated, with an inter-population mean and standard error (95% confidence) calculated for each energy band.

2.4. Shielding evaluation

The optimised and simplified layered shield designs are evaluated using the R_{TF} metric in three different scenarios: shielding the detector crystal in free space, shielding the detector crystal in a simplified model of the biological beamline room, and shielding the PCB and detector electronics combined with the optimised detector shielding strategy in the same simplified beamline/room model.

2.4.1. Free-space configuration (air)

In the free-space configuration, the room is not modelled and the phantom and detector are placed in air, as in our previous work [3]. The detector model is based on the previously-simulated design, consisting of a scintillator or a high density semiconductor crystal, without any PCB or electronic components. The target is irradiated with SOBP60 carbon and helium ion beams, and the detector volume is surrounded by either no shielding, the fully-optimised shielding solution, or the simplified shielding solution; activation and R_{TF} with temporal masking are evaluated for each case and the results are compared.

2.4.2. Closed-space configuration (including the beamline model)

In the closed-space configuration, neutron scattering from the room and the biological beamline at HIMAC are also included in the simulation model [27]. Only the SOBP60 carbon ion beam was simulated, since the model for the helium beam has not yet been validated. In addition to the full beamline model, brass collimators and downstream wall, floor, and ceiling surfaces were added to investigate the influence of scattering on the false positive counts recorded in the detector.

To analyse the directional variation of the neutron fluence around the detector, neutrons entering a 25 cm scoring cube surrounding the detector were recorded and evaluated (Figure 2(a)). The faces of this cube have been labelled 1 to 6, and the spectra of the neutrons entering the cube (divided into 400 logarithmically-spaced energy bins) with and without the walls, floor and ceiling of the room were compared.

R_{TF} and detector activation are evaluated for the three shielding configurations (no shielding, the full set, and the simplified set) over increasing irradiation times, without temporal masking.

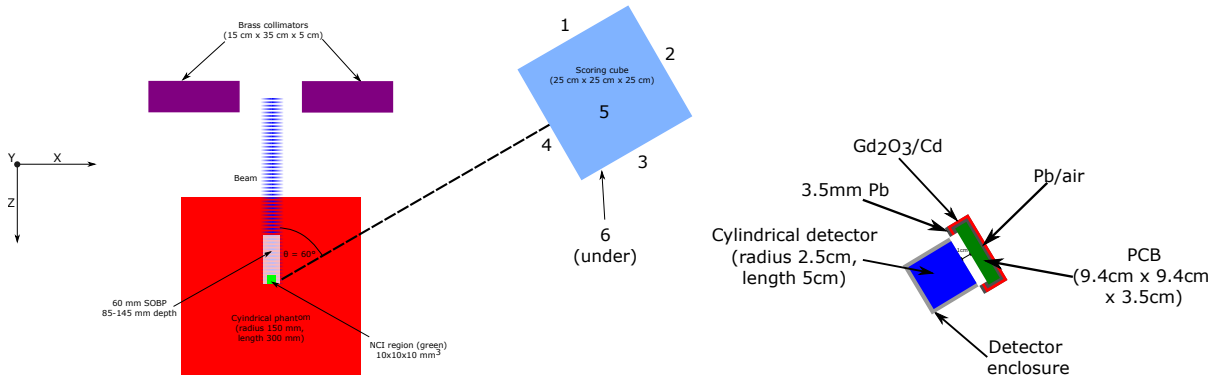

(a) Phantom and scoring cube.

(b) Detector configuration with PCB shielding.

Figure 2: Schematics for the neutron background and PCB shielding simulations. Figure 2(a) contains the scoring cube around the detector module. Figure 2(b) illustrates the detector and its associated PCB, housed within its shield (both of which are surrounded by the scoring cube).

2.4.3. PCB shielding with the closed-space configuration / beamline model

Finally, the impact of shielding the PCB stack and detector electronics on R_{TF} was investigated. False positives originating from photons created in the PCB, as observed in our previous work [4], are generated from neutron capture interactions with the boron in the PCB material. Two scenarios were considered: no PCB shielding and a two-component shield consisting of Gd_2O_3 or cadmium, and lead.

The 9.4 cm × 9.4 cm × 3.5 cm PCB stack[4] was positioned directly behind the detector crystal [17, 4]. As with the BeNEdiCTE system, the PCBs are composed of FR-4 material containing epoxy resin and "E" grade glass fibre with approximately 0.2-0.3% ^{10}B by mass [28]. To minimise the number of false positives, the PCB shielding was designed to be as thin as practically possible, so that neutrons are not scattered back towards the detector. In this case, less importance was placed on thermalising intermediate energy neutrons, and hence no polyethylene or similar moderating material was included in the shielding configurations. Therefore, the shield materials were restricted to Gd_2O_3 or cadmium and lead, which are able to block most of the thermal neutrons which contribute to false positives (and hence which degrade R_{TF}).

An iterative study of Gd_2O_3/Cd of different thicknesses with either 3.5 mm of either lead (1 half value layer, HVL, at 478 keV) or air was conducted for shielding the electronics behind the detector. The shield surrounded the PCB as shown in Figure 2(b), with an additional HVL of lead placed on the outer side of the neutron capture layer next to the crystal. A 1 cm^3 volume of air was also placed between the detector crystal and the PCB to allow space for connecting the components.

The change in the number of false positives created due to neutron capture in either the PCB or shielding was determined and, as in the initial shielding study, the R_{TF} metric was evaluated for each of the different PCB shielding configurations. The optimal design was combined with the best-performing detector shielding obtained from the closed space configuration (Section 2.4.2) - that is, without shielding, with optimised shielding or with simplified shielding.

3. Results

3.1. Single layer shielding evaluation

The Matlab optimiser was run with increasing maximum composite thicknesses of 1 to 10 cm, resulting in the shielding configurations listed in Table 2.

The estimated ratios of transmitted neutron fluence to incident neutron fluence in each energy band obtained from the optimiser as well as the actual ratios obtained from corresponding Geant4 simulations for each of the shield

[4]The 3.5 cm thickness reflects the volume occupied by multiple stacked PCB layers and the electronic components mounted on them.

Table 2: Summary of the shielding configurations with increasing total thickness.

Configuration	Thickness (cm)							
	Polyethylene	**Polycarbonate**	**Gd_2O_3**	**Hf**	**Gd**	**W**	**Al**	**Total**
1	-	-	0.25	0.49	0.26	-	-	1.00
2	-	-	0.59	0.81	0.60	-	-	2.00
3	0.19	0.14	0.82	1.01	0.83	-	-	3.00
4	0.56	0.51	0.92	1.10	0.92	-	-	4.00
5	0.93	0.88	1.01	1.18	1.01	-	-	5.00
6	1.30	1.24	1.10	1.26	1.10	-	-	6.00
7	1.67	1.61	1.19	1.34	1.19	-	-	7.00
8	1.93	1.87	1.25	1.40	1.25	0.30	-	8.00
9	2.02	1.96	1.28	1.42	1.28	1.03	-	9.00
10	2.12	2.06	1.30	1.44	1.30	1.71	0.07	10.00

Table 3: Composition of fully-optimised and simplified shields.

Configuration	Thickness (cm)						
	Polyethylene	**Polycarbonate**	**Gd_2O_3**	**Hf**	**Gd**	**Pb**	**Total**
Full set	1.30	1.24	1.10	1.10	1.26	1.17	7.17
Simplified set	5.00	-	1.00	-	-	1.17	7.17

configurations listed in Table 2 are shown in Figure 3. Since the neutron ratios in the thermal band were consistently low for each shielding configuration, this band is excluded from the figures. It is assumed that the presence of even thin layers of materials with high thermal neutron capture cross-section would offer sufficient shielding in this energy band.

Based on the simulation results, a total shield thickness of 6 cm was determined to be optimal (since it minimises the weighted total number of neutrons reaching the detector). An extra 1 TVL of lead (1.17 cm) was added for shielding against photons. With the inclusion of this layer, the final fully-optimised shield configuration chosen for investigation is as listed in the first row of Table 3. A simplified configuration consisting only of polyethylene (for neutron moderation), Gd_2O_3 (for neutron capture) and 1.17 cm of lead (1 TVL) was also devised using the optimiser. The neutron fluence ratios for these configurations show a reduction in neutron fluence of more than 50% for all bands below 100 keV compared to the no-shielding case.

3.2. Free space configuration (air)

3.2.1. Comparison of R_{TF}

The R_{TF} values for different temporal masks are presented in Figure 4 for both carbon and helium ion beams. These plots correspond to the shortest irradiation time of 1 μs, which consistently resulted in the highest R_{TF} (see Supplementary Materials for R_{TF} values for the remaining irradiation times).

The optimal timing masks for the carbon ion beam are above 70 ns for all shielding configurations, while for helium, the R_{TF} continues to rise with increasing timing mask and no shielding, until a decrease is observed above 120 ns.

With the CdTe detector and carbon ion beam, the highest R_{TF} (0.53 ± 0.02) is achieved with a timing mask duration of 80 ns with no shielding. The shielded configurations result in a reduction of more than 50% in R_{TF} (0.20 ± 0.01 and 0.16 ± 0.02 for the full and simplified sets, respectively), suggesting that a bare detector is the best choice to maximise R_{TF}.

For the helium beam, the CdTe detector without shielding yields a maximum R_{TF} of 1.05 ± 0.09, compared to 0.20 ± 0.05 and 0.13 ± 0.04, for the full and simplified shielding sets, respectively [5].

[5] These results correspond to a temporal mask duration of 120 ns.

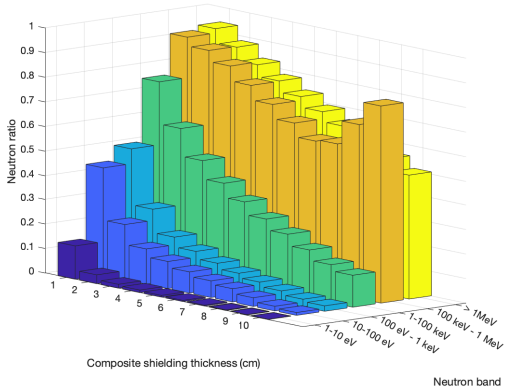

(a) Optimiser ratios, 1-10 eV in the foreground.

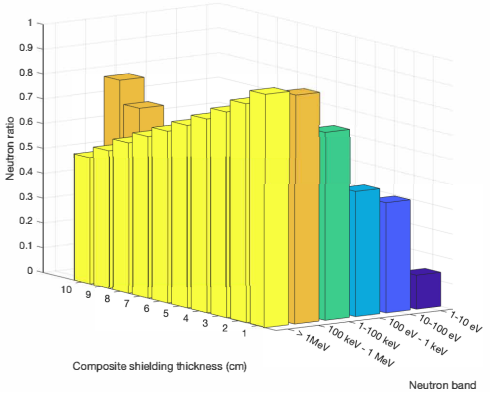

(b) Optimiser ratios, > 1 MeV in the foreground.

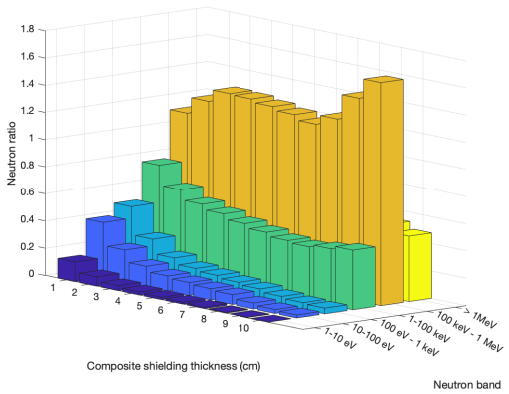

(c) Geant4 ratios, 1-10 eV in the foreground.

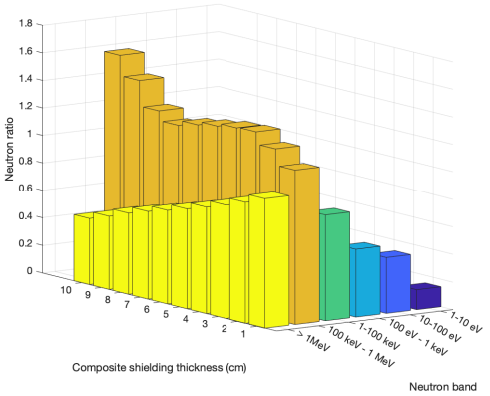

(d) Geant4 ratios, > 1 MeV in the foreground.

Figure 3: Ratios of transmitted to incident neutrons in each energy band for the optimised configurations (in thickness increments of 1 cm, shown on the y-axis), as estimated by the optimiser ((a) and (b)) and as evaluated by Geant4 simulations of the shield configurations ((c) and (d)) over each band (with the exception of thermal neutrons). Each colour represents a different neutron energy band (shown on the x-axis).

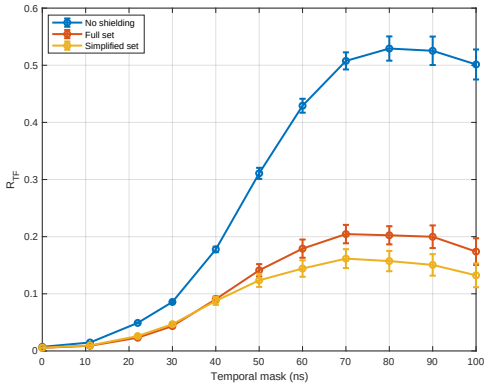

(a) CdTe; carbon ion beam

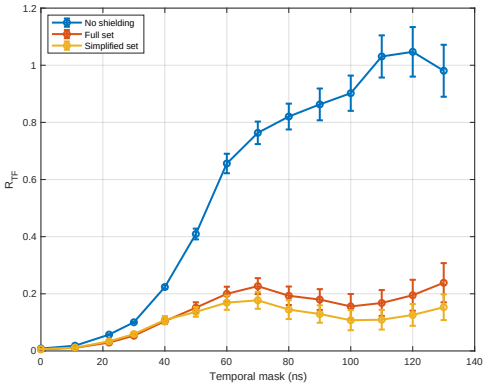

(b) CdTe; helium ion beam

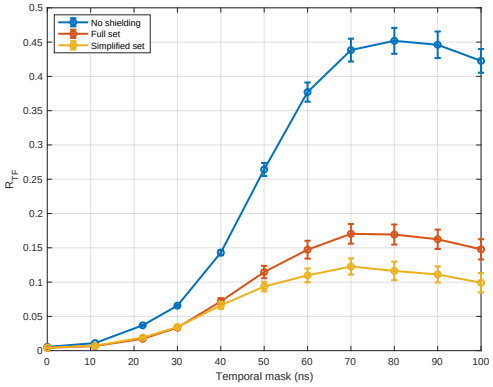

(c) CZT; carbon ion beam

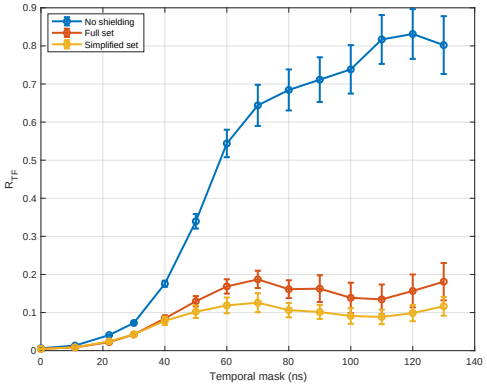

(d) CZT; helium ion beam

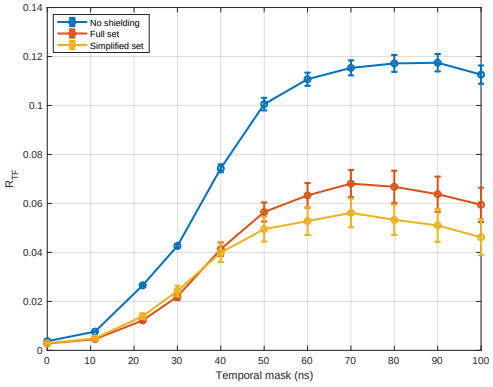

(e) $LaBr_3$; carbon ion beam

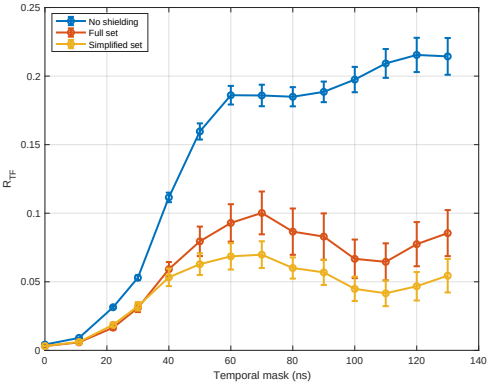

(f) $LaBr_3$; helium ion beam

Figure 4: R_{TF} for each detector material, shielding configuration and ion beam, plotted against increasing temporal mask duration. The plots on the left are for the carbon ion beam, while those on the right are for the helium ion beam. The ratios for the no-shielding case are shown in blue, the fully optimised shield in red and the simplified shielding set in yellow.

3.2.2. Detector activation

The energy deposition from neutron-induced activation in the detector (recorded more than 4 days after irradiation) is shown in Figure 5 for both carbon and helium ion beams. The shielded configurations consistently exhibit a higher number of counts due to neutron activation compared to the unshielded case, with characteristic decay energies observed for each detector material.

For the CdTe detector and carbon ion beam, the 336 keV activation line from ^{115}Cd decay (half life: 53.5 hours [29]) shows an increase of 18.5% and 8.9% in intensity for the simplified and full shielding sets, respectively, compared to no shielding. Similar increases are observed for the helium ion beam and other detector materials.

For CZT, there are multiple spectral peaks corresponding to cadmium activation, including the ^{115}Cd decay peak at 336 keV, a high-intensity peak at 88 keV from the decay of ^{109}Cd, a 245 keV line corresponding to ^{111m}Cd and a 1.123 MeV line from ^{63}Zn decay [29]. With the $LaBr_3$ detector, the increase in energy deposition for the shielded detectors is even more pronounced, with the energy spectrum for the no-shielding case sitting consistently below the shielding spectra at all enrgies. The activation peaks observed with this detector include the highest intensity line at 1.596 MeV from ^{140}La [29].

3.3. Closed space configuration (including the beamline model)

3.3.1. Neutron fluence incident on the detector

The spectra of neutrons incident on each face of the scoring cube surrounding the detector (see Figure2(a)) and the total neutron fluence arriving at the scoring cube with and without concrete walls/floor/ceiling are plotted in Figure 6.

A clear difference in the neutron spectra is observed depending on the detector side; each side exhibits a peak at thermal energies, but the fast neutron fluence is much greater for faces directed towards the beamline and phantom (especially Face 4, which faces the phantom). Scattering from the walls (Figure 6(b)) contributes to the increased fluence across all energies compared to the geometry without walls, emphasising the importance of including the walls in subsequent simulations.

3.3.2. Comparison of R_{TF}

Figure 7 presents R_{TF} as a function of different irradiation times in the closed-space configuration (without the PCB; the beam is carbon ion SOBP60). As in the previous free-space investigation, the no-shielding case exhibits the highest R_{TF} for all detector materials, followed by the full and simplified sets. For all detector materials, R_{TF} converges to a plateau after 100 μs as neutrons thermalise and interact with the detector and surrounding shielding over time.

3.3.3. Detector activation

Figure 8 shows the energy deposition spectra (10 keV linearly-spaced energy bins from 0 MeV to 2 MeV) inside the detector from events occurring later than 4 days post-irradiation. For each detector in the closed-space configuration, activation is higher without shielding. This is the opposite to what was revealed with the free-space configuration.

3.4. Shielding investigation with PCB modelling

The energy deposition in each of the three detector materials with and without the PCB included in the simulation model is shown in Figure 9. No temporal mask is used during irradiation.

3.4.1. Impact of PCB shielding on false positive rate and R_{TF}

Table 4 shows the number of false positives originating in the PCB for each configuration.

The Gd_2O_3 shields achieve a greater decrease in the number of false positives due to neutron captures in the PCB compared to the cadmium shields. By this metric, the best-performing shield is 2 mm of Gd_2O_3 plus 3.5 mm of lead, which results in a 92% decrease in PCB-originating false positives compared to the no-shielding configuration for CdTe.

Table 5 presents the values of R_{TF} obtained for different PCB shielding configurations in conjunction with an unshielded detector. The uncertainties are largely consistent for each detector material, since the greatest contribution to uncertainty in R_{TF} is the number of true positives, which is independent of the PCB shielding configuration.

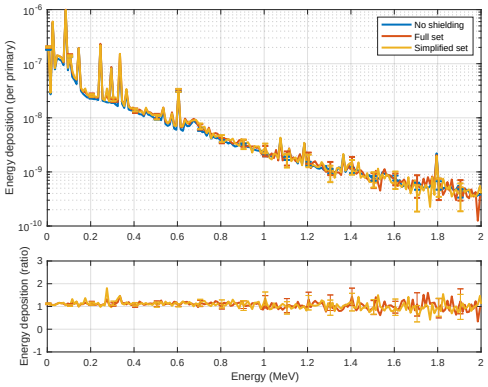

(a) CdTe; carbon ion beam

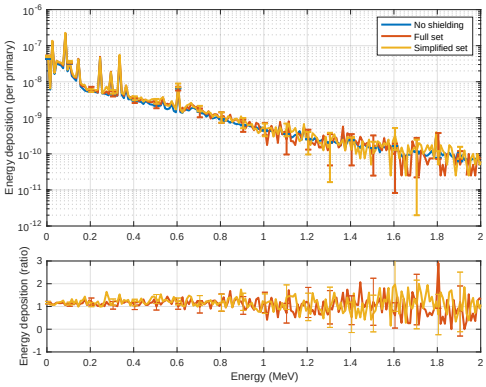

(b) CdTe; helium ion beam

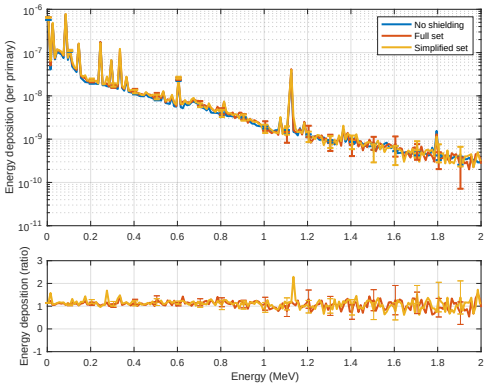

(c) CZT; carbon ion beam

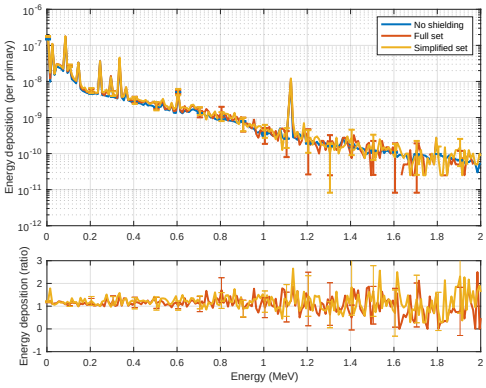

(d) CZT; helium ion beam

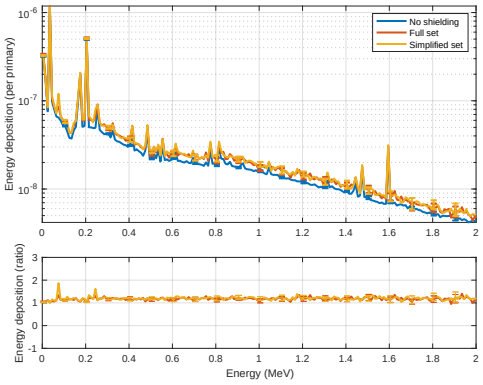

(e) $LaBr_3$; carbon ion beam

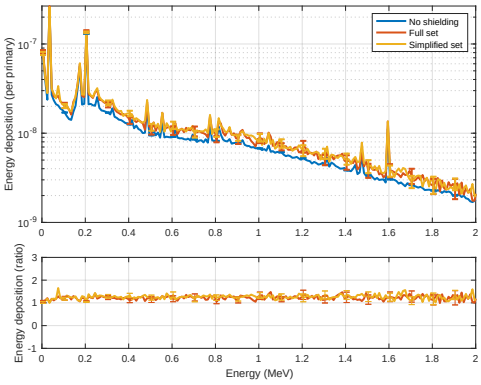

(f) $LaBr_3$; helium ion beam

Figure 5: Energy deposition due to neutron activation of different detector materials following irradiation (upper plot) and the ratio to the no-shielding case (lower plot). The results for carbon ions are shown on the left, while those for helium ions are shown on the right. The blue line denotes the results for the no-shielding case, while red denotes the full set and yellow the simplified set.

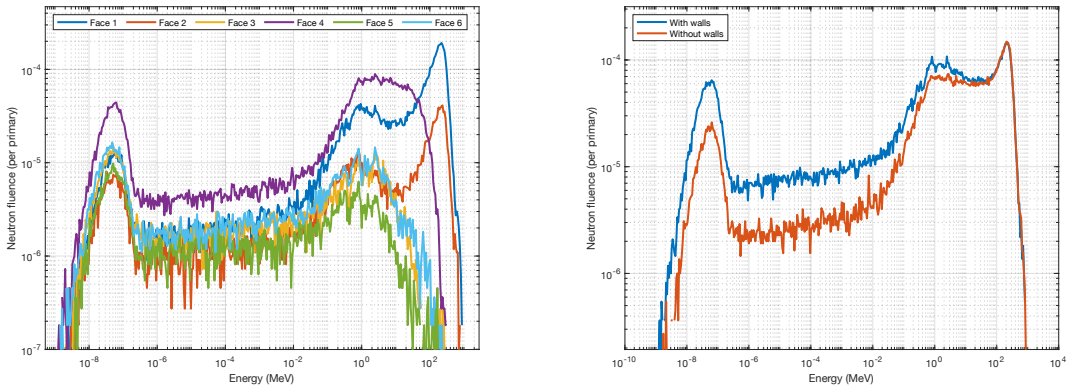

(a) Neutrons incident on each side of detector scoring cube (with concrete walls/floor/ceiling present).

(b) Aggregate neutron spectra incident on the detector scoring cube with and without concrete walls/floor/ceiling present.

Figure 6: Neutron fluence on the detector scoring cube; the neutron spectra scored on each face of the cube surrounding the detector when simulated in the presence of concrete walls/floor/ceiling are plotted in Figure 6(a), while a comparison between the total neutron spectra incident on the scoring cube with and without concrete walls/floor/ceiling present is shown in Figure 6.

Table 4: False positive counts from photons originating in the PCB or shielding, for different shielding configurations with the PCB modelled.

PCB Shielding	**False positives from the PCB**			**False positives from the shielding**		
	CdTe	**CZT**	**$LaBr_3$(Ce)**	**CdTe**	**CZT**	**$LaBr_3$(Ce)**
No shielding	14483 ± 55	13120 ± 49	14874 ± 63	0 ± 0	0 ± 0	0 ± 0
3.5 mm lead, 2 mm Gd_2O_3	1213 ± 20	1131 ± 15	2533 ± 22	3185 ± 27	3926 ± 37	6026 ± 30
3.5 mm lead, 1 mm Gd_2O_3	1455 ± 14	1344 ± 17	2740 ± 27	2840 ± 21	3455 ± 18	5345 ± 33
3.5 mm lead, 2 mm Cd	1293 ± 18	1186 ± 15	2623 ± 18	4328 ± 21	5522 ± 24	8693 ± 44
3.5 mm lead, 1 mm Cd	1480 ± 17	1378 ± 18	2733 ± 34	3934 ± 27	5025 ± 33	7903 ± 36
3.5 mm air, 1 mm Gd_2O_3	1616 ± 14	1490 ± 21	2912± 15	2587 ± 27	3168 ± 24	4744 ± 34
3.5 mm air, 1 mm Cd	1611 ± 18	1496 ± 14	2913± 16	3909 ± 29	5092 ± 31	7931± 39

With the PCB present, R_{TF} is lower than for the no-PCB simulations with limited irradiation times and modelled temporal nano-structure, indicating that the detector activation and the detection of particles with longer arrival times contribute to the increased number of false positive counts.

The addition of shielding of any kind around the PCB increases R_{TF}, with the best result, a 21% improvement in R_{TF} relative to the unshielded PCB case, achieved with 1 mm of Gd_2O_3.

For the CdTe and CZT detectors, R_{TF} increases by 10-21% in every shielded configuration, with the cadmium shield providing a smaller improvement compared to Gd_2O_3. The increase in selectivity with shielding for $LaBr_3$ is smaller at 4-8%, likely due to its inferior energy resolution, which leads to a greater number of false positive counts.

4. Discussion

For both ion beams in the free space model, the no-shielding configuration exhibits the highest R_{TF}, followed by the full set and the simplified set. The CdTe detector outperforms the CZT detector and $LaBr_3$(Ce) detectors, likely due to its superior detection efficiency and energy resolution. The shielded configurations result in a reduction of more than 50% in R_{TF} (0.20 ± 0.01 and 0.16 ± 0.02 for the full and simplified sets, respectively, with this detector), suggesting that a bare detector is the best choice to maximise R_{TF}.

The increased activation with shielding is likely due to fast neutrons and the thermalisation of high-energy neutrons in the surrounding shielding without subsequent capture by other elements of the shield. Overall, the inclusion of

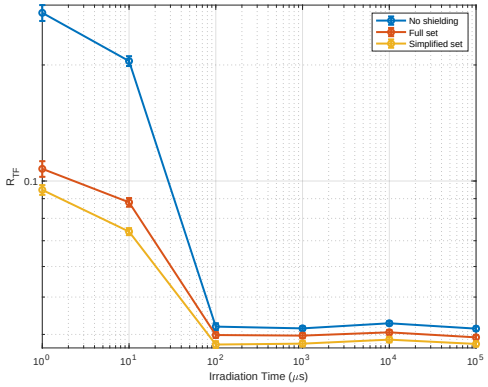

(a) CdTe detector

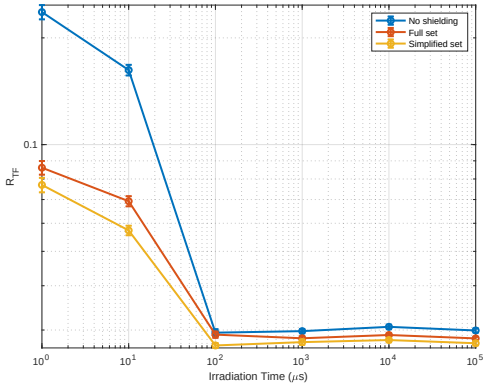

(b) CZT detector

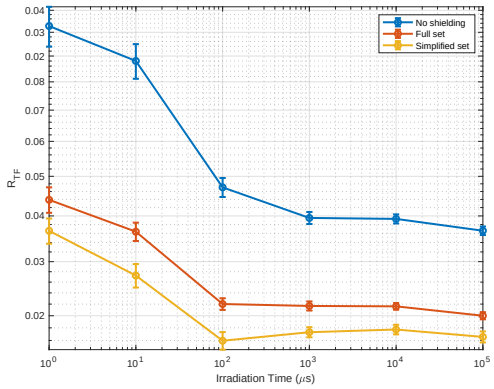

(c) $LaBr_3$ detector

Figure 7: R_{TF} obtained from the carbon ion closed-space simulation, with increasing irradiation times and no temporal mask. Blue denotes no shielding, red the full shield set and yellow the simplified shielding set.

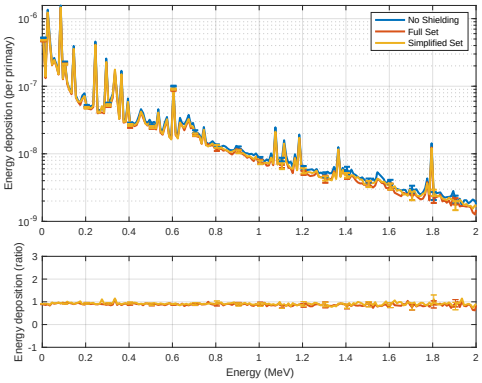

(a) CdTe detector

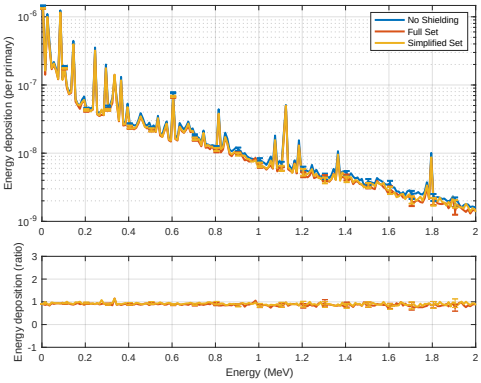

(b) CZT detector

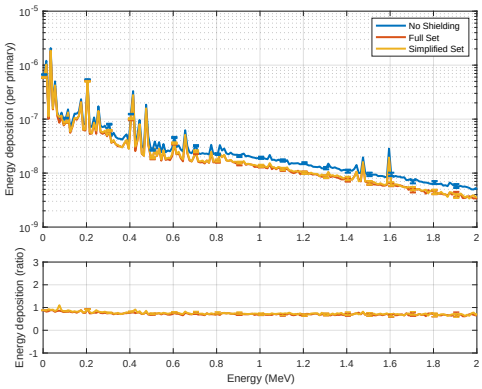

(c) $LaBr_3$ detector

Figure 8: Energy deposition due to activation of the detector following irradiation by the carbon ion beam with beamline neutrons (upper plot) and the ratio of energy deposition with the full and simplified shields to energy deposited with no shielding case (lower plot). Blue denotes the no shielding case, red the full shield set and yellow the simplified set.

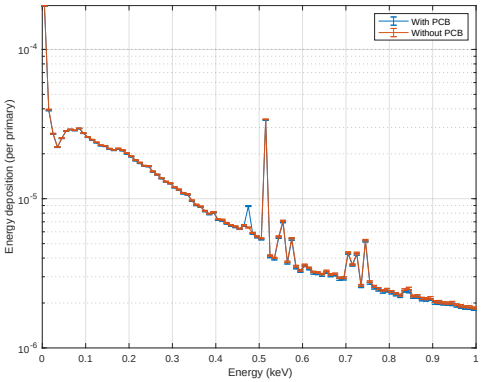

(a) CdTe detector

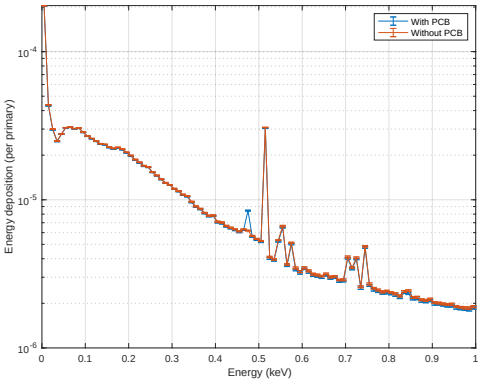

(b) CZT detector

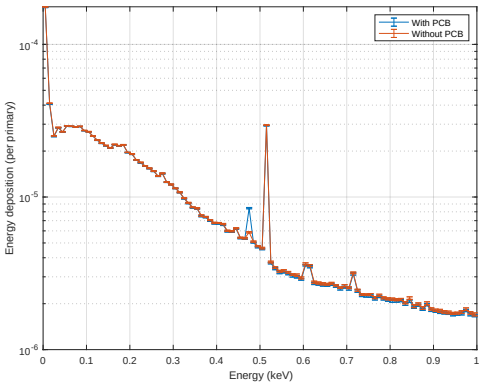

(c) $LaBr_3$ detector

Figure 9: Energy deposition with and without the PCB for each detector with no shielding. Red denotes energy deposition in the detector model without the PCB, while results for the model including the PCB are shown in blue.

Table 5: R_{TF} for different PCB shielding configurations (with the detector crystal unshielded).

PCB Shielding	**R_{TF}($\times 10^{-2}$)**		
	CdTe	**CZT**	**$LaBr_3$(Ce)**
No shielding	1.077 ± 0.013	0.865 ± 0.009	0.661 ± 0.007
3.5 mm lead, 2 mm Gd_2O_3	1.295 ± 0.016	0.980 ± 0.010	0.707 ± 0.008
3.5 mm lead, 1 mm Gd_2O_3	1.297 ± 0.016	0.984 ± 0.010	0.711 ± 0.008
3.5 mm lead, 2 mm Cd	1.264 ± 0.016	0.956 ± 0.010	0.687 ± 0.008
3.5 mm lead, 1 mm Cd	1.270 ± 0.016	0.959 ± 0.010	0.691 ± 0.008
3.5 mm air, 1 mm Gd_2O_3	1.301 ± 0.016	0.988 ± 0.010	0.715 ± 0.008
3.5 mm air, 1 mm Cd	1.270 ± 0.016	0.959 ± 0.010	0.691± 0.008

shielding does not reduce activation, but rather increases energy deposition in the detector.

We hypothesise that while the inclusion of side shielding does not have a measurable impact on the number of true positives, it increases the number of false positives, likely due to neutron interaction and Compton scattering in the shielding material, and hence the highest R_{TF} values are consistently observed for bare detectors. This observation strongly suggests that not only is there no benefit to shielding the detector crystal itself, the use of such a shield degrades the critical performance metric of true to false detections, and therefore is not recommended.

With the inclusion of the background neutrons in the closed space configuration, the selectivity of the detector is much lower. As the irradiation times increase, R_{TF} rapidly decreases to a value almost at least half of that observed in the simulation of the free space. The CdTe detector exhibits the best R_{TF}, followed by the CZT and $LaBr_3$(Ce), which is consistent with the results obtained in the free-space simulation. The additional false positives from neutron interactions in and around the detector significantly degrade R_{TF}, even with shielding.

The greater number of false positives detected in the shielded cases suggests that neutrons undergo inelastic interactions in the shielding layers, and the resulting gamma photons are not sufficiently attenuated by the final lead layer. Neutron scattering in these materials, which otherwise would miss the detector crystal, may also contribute to the increased rate of false positives.

The investigation of detector activation in the closed-space configuration revealed some important findings. Since the activation due to the neutrons from the phantom (see Section 3.2.2) is greater *with* shielding, neutron shielding behind the detector crystal could be valuable in this case since it would attenuate the scattered beamline neutrons. However, it is still recommended to omit shielding around the detector crystal even in this case.

As expected, the energy deposition in the detector at 478 keV is much higher with the addition of the PCB to the model; the increased number of false positive counts from neutron capture inside the boron of the PCB will result in a decrease in R_{TF}. This supports the necessity of adding a shield around the back of the detector to reduce neutron capture events in the PCB and consequently minimise the rate of false positives in the detector.

In the PCB shielding investigation, the overall effect of the lead layer on R_{TF} appears to be largely negligible, with a statistically insignificant difference in R_{TF} obtained with 3.5 mm of lead and and 3.5 mm of air between the 1 mm Gd_2O_3 shielding layer and the PCB. This is because the number of false positives due to photons originating in the shielding layer increases slightly more than the decrease in the number of false positives from PCB boron neutron capture.

It is possible that some thermal neutrons that would otherwise escape are reflected back by the lead and go on to interact with the Gd_2O_3 or cadmium layer, thus emitting additional neutron capture photons and increasing the false positive count. The lead may also result in additional Compton scattering of neutron capture photons from the PCB or shield, increasing the likelihood of interaction with the detector. The net result is that the addition of a layer of lead does not improve R_{TF} (and, in fact, degrades it slightly).

We note that cadmium foils have been used successfully for the BeNEdiCTE detector to reduce false positives from the PCB [30, 31]. In this case, the detector and electronics were surrounded by 0.5-4 mm thick cadmium during experiments with a thermal neutron beam. The position of the detector relative to the beamline, as well as the absence of projectile fragmentation (as compared to the heavy ion beams used in this simulation study), are the most likely reasons for the differing performance of this shielding.

Overall, the best-performing detector material was CdTe, with an 80 ns temporal mask. For optimal performance, shielding the PCB with 1 mm Gd_2O_3 is recommended, as it results in an improvement in R_{TF} of 4-21% depending on the detector material. This improvement justifies the expense and complexity of adding the shield. However, shielding the scintillator crystal or semiconductor detector itself appears to only degrade the specificity of the detector while generally contributing to an increased degree of neutron activation of the detector, and is therefore not recommended. Notably, adding a layer of lead in addition to the Gd_2O_3 shield provided no additional benefit.

While Gd_2O_3 proved effective due to its high neutron capture cross-section, future investigations should consider alternative shielding materials. Our optimisation process, which included a penalty for photon production, balanced neutron capture efficiency with minimisation of gamma emissions. The lack of improvement in R_{TF} with additional shielding suggests that gamma emissions from Gd_2O_3 do not significantly contribute to false positives in our system. Alternative materials like ^{6}Li, despite lower (or no) gamma production, present challenges due to their lower neutron capture cross-section (940 barns for 6Li vs 49,000 barns for natural gadolinium), potentially requiring thicker shields that could constrain clinical deployment.

Further investigation into shielding configurations at a greater distance from the detector is recommended, particularly in the presence of a high neutron fluence from the beamline. The decrease in R_{TF} for most shielding configurations compared to the bare detector might be caused by the close proximity of the shielding materials to the detector. As such, additional consideration of neutron and photon scattering inside the shielding materials is important for future work.

5. Conclusions

This study investigated the potential benefits of various shielding configurations for increasing the ratio of true positives to false positives (R_{TF}) of a neutron capture detection and discrimination detection system for ^{10}B NCEPT. The best detector, irradiation time and temporal mask were determined to be CdTe with a 1 μs irradiation period and 80 ns temporal mask in the ideal case with no background neutrons from the beamline. Shielding consistently decreased in R_{TF} for all detectors, and resulted in increased detector activation.

It is important to note that the dimensions of the semiconductors in this study have contributed to the high detection efficiency of the system. All results obtained in this work are for a 5 cm thick total detector volume. For the case of CdTe or CZT detectors, these results can therefore be applied only in cases where multiple detector layers have been electronically coupled. As the $LaBr_3$(Ce) scintillator crystal is commercially available in large sizes, this scintillator-based detector is still the most practical choice for neutron capture photon detection.

The results suggest that a bare detector would be the best choice for the highest R_{TF} in environments with minimal background. For the CdTe detector with an 80 ns temporal window, R_{TF} decreased from 0.53 ± 0.02 for the bare detector to 0.20 ± 0.01 and 0.16 ± 0.02 for the fully-optimised and simplified shielding sets. This decrease R_{TF} by more than half demonstrates the effect of increased false positive counts resulting from the inclusion of shielding.

The activation of the detector, represented by the energy depositions from activation 4 days post-irradiation, increased following the inclusion of shielding for all detectors and beam configurations in free-space. For the activation lines of interest, there was a maximum increase of approximately 32% for the CdTe detector, with the simplified shielding configuration resulting in an even greater increase of 81%. This finding further supports the use of a bare detector module in a low-background environment.

In mixed-field environments with background from scattering and neutron interactions, a small amount of a high neutron capture cross-section material (such as Gd_2O_3) around the PCB is an effective way to increase R_{TF}, if the PCB is fabricated from a conventional epoxy/glass-fibre composite. All shielding configurations showed a decrease of up to 89% in the number of false positive counts originating from the PCB. However, the addition of shielding also introduced a new source of false positives due to neutron interactions with the shield, limiting the improvement in R_{TF} that could be obtained.

The optimal configuration was found to be 1 mm Gd_2O_3 surrounding the PCB, which increased R_{TF} of the CdTe detector by approximately 21%. It is recommended that the greatest potential improvement in R_{TF} would be obtained through reduction or elimination of boron in the PCB and associated electronics through substitution of a glass-free PCB substrate such as Kapton.

Due to the different energies of the neutron capture photons present from interactions with ^{10}B and ^{157}Gd, the optimal detector materials and shielding strategies may be different if a ^{157}Gd-based NCA is used. In this case, the

optimal shield would include boron, since the much lower energy of the neutron capture prompt gamma photons would be well below the detection energy window.

This study highlights the importance of carefully considering the influence of each element of the shielding configuration on detector performance. In an environment with low levels of neutron contamination in the ion beam or neutron scattering in the room, the best detector performance is achieved without additional shielding around the detector crystal. In contrast, in a mixed-field environment, a modest shield (such as 1 mm Gd_2O_3) is recommended around the detector PCB if it is known to contain boron.

Author contributions statement

Ms M.K. performed all Monte Carlo simulations for shielding and analysed all data obtained throughout this study. She generated all results and contributed to the writing of the manuscript. Dr A.C. assisted in the development of the Monte Carlo simulation model. Ms A.C. provided the specifications of the BeNEdiCTE system for simulation and contributed to the proof-reading of the manuscript. Dr D.B. carried out the Monte Carlo beam line simulation for inclusion in the closed-space configuration. Dist Prof A.R. provided feedback on the manuscript and guidance on its development. Prof M.C. and Prof C.F. developed the BeNEdiCTE detection system, provided guidance on the methods and contributed to proof-reading. A/Prof D.F. contributed to the interpretation of the results and assisted in manuscript preparation. Prof S.G. assisted in the development of the methods and contributed to proof-reading. A/Prof M.S.-N. provided leadership for the project and assisted in the data analysis. She contributed to the writing, proof-reading and composition of this manuscript.

Declaration of competing interest

The author(s) declare no competing interests.

Acknowledgements

This research was conducted with the support of an Australian Government Research Training Scholarship and an Australian Institute of Nuclear Science and Engineering (AINSE) Ltd. Residential Student Scholarship (RSS). All simulations were conducted through the use of the high-performance computing resources at the National Computational Infrastructure (NCI) and the MASSIVE cluster.

Data Availability

All data generated or analysed during this study are included in this published article or are available from the corresponding author upon reasonable request.

References

[1] N. Howell, R. J. Middleton, F. Sierro, N. A. Wyatt, A. Chacon, B. H. Fraser, K. R. Bambery, E. Livio, C. Dobie, J. J. Bevitt, J. Davies, A. Dosseto, D. R. Franklin, U. Garbe, S. Guatelli, R. Hirayama, N. Matsufuji, A. Mohammadi, K. Mutimer, L. M. Rendina, A. B. Rosenfeld, M. Safavi-Naeini, Neutron capture enhances dose and reduces cancer cell viability in and out of beam during helium and carbon ion therapy, International Journal of Radiation Oncology*Biology*Physics (Mar. 2024). doi:10.1016/j.ijrobp.2024.02.052.
URL http://dx.doi.org/10.1016/j.ijrobp.2024.02.052

[2] M. Safavi-Naeini, A. Chacon, S. Guatelli, D. R. Franklin, K. Bambery, M.-C. Gregoire, A. Rosenfeld, Opportunistic dose amplification for proton and carbon ion therapy via capture of internally generated thermal neutrons, Scientific Reports 8 (1) (Nov. 2018). doi:10.1038/s41598-018-34643-w.
URL https://doi.org/10.1038/s41598-018-34643-w

[3] A. Chacon, M. Kielly, H. Rutherford, D. R. Franklin, A. Caracciolo, L. Buonanno, I. D'Adda, A. Rosenfeld, S. Guatelli, M. Carminati, C. Fiorini, M. Safavi-Naeini, Detection and discrimination of neutron capture events for NCEPT dose quantification, Scientific Reports 12 (1) (Apr. 2022). doi:10.1038/s41598-022-09676-x.
URL https://doi.org/10.1038/s41598-022-09676-x

[4] M. Kielly, A. Caracciolo, A. Chacon, J. Vohradsky, D. Di Vita, A. Hamato, H. Tashima, D. R. Franklin, T. Yamaya, A. Rosenfeld, M. Carminati, C. Fiorini, S. Guatelli, M. Safavi-Naeini, First experimental demonstration of real-time neutron capture discrimination in helium and carbon ion therapy, Scientific Reports 14 (1) (2024) 2601, number: 1 Publisher: Nature Publishing Group. doi:10.1038/s41598-024-52162-9.
URL https://www.nature.com/articles/s41598-024-52162-9

[5] J. Kelley, J. Purcell, C. Sheu, Energy levels of light nuclei a= 12, Nuclear Physics A 968 (2017) 71–253. doi:10.1016/j.nuclphysa.2017.07.015.
URL https://doi.org/10.1016/j.nuclphysa.2017.07.015

[6] R. D. Bello, P. M. Martins, J. Graça, G. Hermann, T. Kihm, J. Seco, Results from the experimental evaluation of CeBr3 scintillators for 4he prompt gamma spectroscopy, Medical Physics (May 2019). doi:10.1002/mp.13594.
URL https://doi.org/10.1002/mp.13594

[7] D. Tilley, H. Weller, C. Cheves, Energy levels of light nuclei a = 16–17, Nuclear Physics A 564 (1) (1993) 1–183. doi:10.1016/0375-9474(93)90073-7.
URL https://doi.org/10.1016/0375-9474(93)90073-7

[8] G. F. Knoll, Fast Neutron Detection and Spectroscopy, 4th Edition, John Wiley and Sons, Inc, 2010, Ch. 15, pp. 553–593.

[9] E. Bayat, H. Afarideh, F. A. Davani, N. Ghal-Eh, A quality survey on different shielding configurations of gamma ray detector used with a portable PGNAA system, Radiat. Phys. Chem. Oxf. Engl. 1993 120 (2016) 7–11.

[10] Z. Uddin, T. Yasin, M. Shafiq, A. Raza, A. Zahur, On the physical, chemical, and neutron shielding properties of polyethylene/boron carbide composites, Radiat. Phys. Chem. Oxf. Engl. 1993 166 (108450) (2020) 108450.

[11] J. M. Verburg, J. Seco, Proton range verification through prompt gamma-ray spectroscopy, Physics in Medicine and Biology 59 (23) (2014) 7089–7106. doi:10.1088/0031-9155/59/23/7089.
URL https://doi.org/10.1088/0031-9155/59/23/7089

[12] I. M. Kobayashi T, Sakurai Y, A noninvasive dose estimation system for clinical bnct based on pg-spect–conceptual study and fundamental experiments using hpge and cdte semiconductor detectors, Medical Physics 27 (2000) 2124–2132. doi:10.1118/1.128824.

[13] W. Verbakel, F. Stecher-Rasmussen, A γ-ray telescope for on-line measurements of low boron concentrations in a head phantom for bnct, Nuclear Instruments and Methods in Physics Research Section A: Accelerators, Spectrometers, Detectors and Associated Equipment 394 (1-2) (1997) 163–172. doi:10.1016/s0168-9002(97)00667-0.

[14] H. Ithnin, L. N. S. Dahing, N. M. Lip, I. Q. Abd Rashid, E. J. Mohamad, Study on detection geometry and detector shielding for portable PGNAA system using PHITS, IOP Conf. Ser. Mater. Sci. Eng. 298 (2018) 012053.

[15] S. Agostinelli, J. Allison, K. Amako, et al., Geant4 - a simulation toolkit, Nuclear Instruments and Methods in Physics Research Section A: Accelerators, Spectrometers, Detectors and Associated Equipment 506 (3) (2003) 250–303. doi:10.1016/s0168-9002(03)01368-8.
URL https://doi.org/10.1016/s0168-9002(03)01368-8

[16] Geant4 Collaboration, Geant4 material database, http://geant4-userdoc.web.cern.ch/geant4-userdoc/UsersGuides/ForApplicationDeveloper/html/Appendix/materialNames.html, accessed 21 April 2020.

[17] A. Caracciolo, L. Buonanno, D. Di Vita, I. D'Adda, A. Chacon, M. Kielly, M. Carminati, M. Safavi-Naeini, C. Fiorini, Benedicte (boron neutron capture): a versatile gamma-ray detection module for boron neutron capture therapy, IEEE Transactions on Radiation and Plasma Medical Sciences (2022) 1–1doi:10.1109/TRPMS.2022.3154232.

[18] M. Zarifi, S. Guatelli, Y. Qi, D. Bolst, D. Prokopovich, A. Rosenfeld, Characterization of prompt gamma ray emission for in vivo range verification in particle therapy: A simulation study, Physica Medica 62 (2019) 20–32. doi:10.1016/j.ejmp.2019.04.023.
URL https://doi.org/10.1016/j.ejmp.2019.04.023

[19] T. Werner, J. Berthold, F. Hueso-González, T. Koegler, J. Petzoldt, K. Roemer, C. Richter, A. Rinscheid, A. Straessner, W. Enghardt, G. Pausch, Processing of prompt gamma-ray timing data for proton range measurements at a clinical beam delivery, Physics in Medicine & Biology 64 (10) (2019) 105023. doi:10.1088/1361-6560/ab176d.
URL https://doi.org/10.1088/1361-6560/ab176d

[20] Advatech, LaBr3(Ce) - Scintillator Crystal, https://www.advatech-uk.co.uk/labr3_ce.html (2021).

[21] Saint-Gobain Crystals, Lanthinum Bromide LaBr3(Ce), https://www.crystals.saint-gobain.com/products/standard-and-enhanced-lanthanum-bromide (2021).

[22] I. Murata, S. Nakamura, M. Manabe, H. Miyamaru, I. Kato, Characterization measurement of a thick CdTe detector for BNCT-SPECT – detection efficiency and energy resolution, Applied Radiation and Isotopes 88 (2014) 129–133. doi:10.1016/j.apradiso.2014.01.023.
URL https://doi.org/10.1016/j.apradiso.2014.01.023

[23] Advatech, CZT Detectors - Sensors & Integrated Probes, https://www.advatech-uk.co.uk/radiation_czt.html (2021).

[24] S. Yamada, Commissioning and performance of the HIMAC medical accelerator, in: Proceedings Particle Accelerator Conference, IEEE, pp. 9–13. doi:10.1109/pac.1995.504557.
URL https://doi.org/10.1109%2Fpac.1995.504557

[25] T. Fujimoto, M. Kanazawa, T. Shirai, Y. Iwata, H. Uchiyama, K. Noda, Acceleration of heavy ions with a new RF system at HIMAC synchrotron, Nuclear Instruments and Methods in Physics Research Section B: Beam Interactions with Materials and Atoms 269 (24) (2011) 2886–2890. doi:10.1016/j.nimb.2011.04.029.
URL https://doi.org/10.1016%2Fj.nimb.2011.04.029

[26] A. Altman, J. Gondzio, Regularized symmetric indefinite systems in interior point methods for linear and quadratic optimization, Optimization Methods and Software 11 (1–4) (1999) 275–302. doi:10.1080/10556789908805754.
URL http://dx.doi.org/10.1080/10556789908805754

[27] D. Bolst, L. T. Tran, S. Guatelli, N. Matsufuji, A. B. Rosenfeld, Modelling the biological beamline at HIMAC using geant4, Journal of Physics: Conference Series 1154 (2019) 012003. doi:10.1088/1742-6596/1154/1/012003.
URL https://doi.org/10.1088/1742-6596/1154/1/012003

[28] S. P. Platt, S. August, M. MacLeod, M. J. Anderson, D. Cheneler, S. D. Monk, Thermal neutron absorption in printed circuit boards, IEEE

Transactions on Nuclear Science 68 (4) (2021) 463–469. doi:10.1109/tns.2021.3060864.
URL https://doi.org/10.1109/tns.2021.3060864

[29] L. E. S.Y.F. Chu, R. Firestone, The lund/lbnl nuclear data search, http://nucleardata.nuclear.lu.se/toi/ (1999).

[30] A. Caracciolo, D. D. Vita, L. Buonanno, M. Carminati, N. Protti, S. Altieri, A. Pola, D. Bortot, C. Fiorini, Experimental validation of a spectroscopic gamma-ray detector based on a LaBr3 scintillator towards real-time dose monitoring in BNCT, Nuclear Instruments and Methods in Physics Research Section A: Accelerators, Spectrometers, Detectors and Associated Equipment 1041 (2022) 167409. doi:10.1016/j.nima.2022.167409.
URL https://doi.org/10.1016/j.nima.2022.167409

[31] G. Colombo, A. Caracciolo, D. Mazzucconi, G. Borghi, M. Carminati, N. Protti, S. Altieri, S. Agosteo, C. Fiorini, Study of the Thermal Neutron Activation of a Gamma-Ray Detector for BNCT Dose Monitoring, Journal of Instrumentation, In press (2024).